

Plastic enhancement mechanism of γ-TiAl//α_2-Ti_3Al lamellar structure via Al_{Ti} antisite defect

Lei Sheng(盛磊), Xiong Zhou(周雄), Qiran Gong(龚琪然), Zhongtao Lu(陆忠涛), Pengcheng Zhai(翟鹏程), Xiege Huang(黄写格), Shiping Wang(王世平), Wenjuan Li(李文娟), Xiaobin Feng(冯骁斌), and Guodong Li(李国栋)
Citation: Chin. Phys. B, 2026, 35 (**7**): 076401. DOI: 10.1088/1674-1056/ae5a10
http://cpb.iphy.ac.cn; http://iopscience.iop.org/cpb

What follows is a list of articles you may be interested in

Insights into the adsorption of water and oxygen on the cubic $CsPbBr_3$ surfaces: A first-principles study

Xin Zhang(张鑫), Ruge Quhe(屈贺如歌), and Ming Lei(雷鸣)
Chin. Phys. B, 2022, 31 (**4**): 046401. DOI: 10.1088/1674-1056/ac3987

The effect of dislocations on the thermodynamic properties of Ta single crystal under high pressure by molecular dynamics simulation

Yalin Li(李亚林), Jun Cai(蔡军), Dan Mo(莫丹), Yandong Wang(王沿东)
Chin. Phys. B, 2018, 27 (**8**): 086401. DOI: 10.1088/1674-1056/27/8/086401

Phase transition, elastic and electronic properties of topological insulator Sb_2Te_3 under pressure: First principle study

Qing Lu(卢清), Huai-Yong Zhang(张怀勇), Yan Cheng(程 艳), Xiang-Rong Chen(陈向荣), Guang-Fu Ji(姬广富)
Chin. Phys. B, 2016, 25 (**2**): 026401. DOI: 10.1088/1674-1056/25/2/026401

RAPID COMMUNICATION

Plastic enhancement mechanism of γ-TiAl//α_2-Ti_3Al lamellar structure via Al_{Ti} antisite defect

Lei Sheng(盛磊)[1,†], Xiong Zhou(周雄)[1,†], Qiran Gong(龚琪然)[2], Zhongtao Lu(陆忠涛)[2], Pengcheng Zhai(翟鹏程)[1,2], Xiege Huang(黄写格)[2], Shiping Wang(王世平)[2], Wenjuan Li(李文娟)[2], Xiaobin Feng(冯骁斌)[2], and Guodong Li(李国栋)[1,2,‡]

[1] *State Key Laboratory of Light Superalloys, Wuhan University of Technology, Wuhan* 430070, *China*

[2] *Hubei Key Laboratory of Theory and Application of Advanced Materials Mechanics, School of Physics and Mechanics, Wuhan University of Technology, Wuhan* 430070, *China*

(Received 9 February 2026; revised manuscript received 20 March 2026; accepted manuscript online 1 April 2026)

Polysynthetically twinned (PST) TiAl consisting of a two-phase (γ and α_2) lamellar structure is an effective microstructural strategy for enhancing mechanical properties, and Al-rich composition is a common phenomenon. However, the effect of the Al_{Ti} antisite defect on the deformation mechanism of the γ-TiAl//α_2-Ti_3Al lamellar structure remains unclear. The deformation mechanisms of the γ//α_2 lamellar structure under pure shear mainly involve three sequential stages: (i) The weaker Ti–Ti and Al–Al metallic bonds induce the "phase boundary (PB) transition". (ii) The stronger Ti–Ti and Al–Al metallic bonds induce the "orientation transition" in γ-TiAl. (iii) The strongest Ti–Al covalent bonds induce the "phase transition" in α_2-Ti_3Al. Introducing an Al_{Ti} antisite defect can weaken the original Ti–Al covalent bonds while generating new Al–Al metallic bonds, which provides an additional slip path and results in excellent enhancement of plasticity. The competition mechanisms between these plastic behaviors can be well explained through generalized stacking fault energy (GSFE) calculations.

Keywords: density-functional theory, TiAl alloys, antisite defects, intrinsic mechanical properties

PACS: 64.70.kd, 31.15.E–, 31.15.es, 61.46.–w

DOI: 10.1088/1674-1056/ae5a10 **CSTR:** 32038.14.CPB.ae5a10

1. Introduction

The aircraft engines and other key components like blades need to withstand harsh conditions, i.e., high temperature, high pressure, high rotational speed, and alternating loads, which underscore the necessity for designing advanced alloys.[1–5] Hence, TiAl alloys are considered ideal lightweight engineering materials due to their low density, high specific strength, high service temperature (650–850 °C), and good oxidation resistance.[6–10] TiAl alloys have broad application prospects in the aerospace field. TiAl-4822 alloys were successfully applied to the low-pressure turbine of the GEnx engine in 2011,[11] and Motoren-und Turbinen-Union (MTU) applied the TiAl-TNM alloy to the Airbus A320neo aircraft in 2016.[12] However, the low ductility at room temperature and low high-temperature strength of TiAl alloys seriously limit their wide application.

The lamellar structure of polysynthetically twinned (PST) TiAl is reported to be the most effective microstructural strategy to synergistically enhance the strength and ductility of TiAl alloys. Chen *et al.*[13] prepared 0°-oriented PST single crystals and conducted tensile tests, which showed excellent room-temperature yield strength (735 MPa) and tensile ductility ($\sim 7.6\%$), while the room-temperature tensile ductility of previously reported TiAl alloys typically exhibits $< 2\%$. Ma *et al.*[14] found that the Ti-46Al-6Nb PST single crystal demonstrates exceptional high-temperature tensile performance, with a ductility of 8.1% and a strength of 668 MPa at 800 °C. PST TiAl lamellar colonies consist of γ phase, α_2 phase, and the γ/α_2 phase boundary, and they have a great influence on the mechanical properties, where the orientation relationship between γ and α_2 phases follows the Blackburn relationship: $\{111\}\gamma \parallel (0001)\alpha_2$, $\langle 1\bar{1}0\rangle\gamma \parallel \langle 11\bar{2}0\rangle\alpha_2$.[15]

In our previous work, we found that the excellent ductility and high strength of γ-TiAl originate from the metallic bonding and covalent bonding, respectively.[16] Chen *et al.*[13] considered that the good ductility of PST single crystals is due to the large number of nanotwins in γ-TiAl. In PST–TiAl alloys, the α_2-Ti_3Al phase tends to be a hard phase known for its limited slip systems, and Goken *et al.* found that the hardness of the α_2 phase is approximately 50% higher than that of the γ phase.[17,18] Chen *et al.*[19] found that PST TiAl single crystals exhibited significantly superior fatigue resistance at 975 °C, and the stacking fault structures observed in the α_2 lamellae played a critical role. It has been reported that the γ/γ twin

[†] These authors contributed equally to this work.

[‡] Corresponding author. E-mail: guodonglee@whut.edu.cn

© 2026 Chinese Physical Society and IOP Publishing Ltd. All rights, including for text and data mining, AI training, and similar technologies, are reserved.

structure always appears in the γ phase due to the low stacking fault energy.[20,21] Xiang *et al.*[22] reported that the γ/γ twin boundary and γ/α_2 phase boundary have a synergistic effect on lamellar TiAl single crystals. However, the chemical-bond-related deformation mechanisms of the two-phase (γ and α_2) PST TiAl lamellae have not been fully considered in essence. In addition, Xu *et al.*[23] found that the contents of Ti and Al are 43.17 at.% and 47.85 at.% in the γ phase, respectively. Li *et al.*[24] found that the contents of Ti and Al are 61.58 at.% and 31.60 at.% in the α_2 phase, respectively. The stoichiometric ratio of Ti and Al atoms in the α_2-Ti_3Al phase is 3:1, while that in γ-TiAl is 1:1.[23] Therefore, hyperstoichiometric (Al-rich) compositions are common during the manufacturing process of PST TiAl, which leads to Al_{Ti} antisite defects.[25–29] It is crucial to understand the effect of Al_{Ti} antisite defects on the chemical-bond-related deformation mechanism of the γ-TiAl/α_2-Ti_3Al lamellar structure.

In this work, the competitive deformation mechanisms of the γ-TiAl/α_2-Ti_3Al lamellar structure with Al_{Ti} antisite defects at the atomic scale are thoroughly investigated based on first-principles calculations. The Al_{Ti} antisite defect preferentially occupies the Al site at the phase boundary in α_2-Ti_3Al (denoted as Al3 in our structural model), as indicated by its lowest formation energy. The deformation mechanisms of the γ/α_2 lamellar structure under pure shear mainly contain three sequential stages: (I) the weaker Ti–Ti and Al–Al metallic bonds induce "phase boundary (PB) transition"; (II) the stronger Ti–Ti and Al–Al metallic bonds induce "orientation transition" in γ-TiAl; and (III) the strongest Ti–Al covalent bonds induce "phase transition" in α_2-Ti_3Al. Moreover, introducing Al_{Ti} antisite defects can weaken the original Ti–Al covalent bond while generating a new Al–Al metallic bond. The "PB transition" can be easily activated with the lowest strength of 3.0 GPa. The "orientation transition" induced by SISF processes (SISF formation, SISF migration, and SISF annihilation) in γ-TiAl and the "phase transition" in α_2-Ti_3Al (Al_{Ti}) with a strength of $\sim$ 5.0 GPa continuously dissipate the strain energy, resulting in excellent ductility. The shear strain of the γ/α_2 lamellar structure (Al_{Ti}) increased to 0.93 from 0.78, contributing to a $\sim$ 19% enhancement in plasticity. The competitive mechanisms between these plastic behaviors can be well explained through GSFE calculations. The results show that the slip energy barriers of "PB transition", "orientation transition" in γ-TiAl, and "phase transition" in α_2-Ti_3Al are 177.0 mJ/m^2, 299.6 mJ/m^2, and 476.6 mJ/m^2, respectively. The slip energy barrier of "phase transition" decreases to 282.7 mJ/m^2 in the interlayer with Al_{Ti} antisite defects. The presence of PB2 strengthens the γ/α_2 lamellar structure with a high slip energy barrier of 1135.0 mJ/m^2.

2. Methodology

All calculations were carried out using the projector augmented wave (PAW) method to describe the interaction between ionic cores and valence electrons within the Vienna *ab initio* simulation package (VASP) through density functional theory (DFT).[30] The Perdew–Burke–Ernzerhof (PBE) exchange–correlation functional within the generalized gradient approximation (GGA) was employed in the DFT calculations.[31] The plane-wave cutoff energy was set to 500 eV for geometry optimization. The electronic convergence and geometry optimization energy criteria were set to 1×10^{-6} eV and 1×10^{-2} eV·Å^{-1}, respectively. For Ti and Al, the valence electrons were treated as $3s^23p^63d^24s^2$ and $3s^23p^1$, respectively. We used the Monkhorst–Pack $8 \times 8 \times 8$ and $6 \times 3 \times 6$ k-point meshes to sample the Brillouin zone for the optimization of the γ-TiAl and α_2-Ti_3Al unit cells, respectively, while a $3 \times 6 \times 1$ Monkhorst–Pack grid was used for the pure shear simulations and GSFE calculations. The detailed description of pure shear calculations through DFT is provided in our previous work.[32–34] We also used the electron localization function (ELF) to classify the chemical bond character, and crystal orbital Hamilton population (COHP) calculations were performed using the LOBSTER code to reveal the strength of chemical bonds of the same type.[35,36] All visualizations for the calculations in this study were performed with the VESTA software.[37]

3. Crystal structure and chemical bonding of γ-TiAl/α_2-Ti_3Al lamellar structure

The crystal structures of γ-TiAl and α_2-Ti_3Al are shown in Figs. 1(a) and 1(b). γ-TiAl crystallizes in the $L1_0$ tetragonal structure, and α_2-Ti_3Al crystallizes in the hexagonal close-packed structure, with space groups $P4/mmm$ (No. 123) and $P6_3/mmc$ (No. 194), respectively. The optimized lattice parameters of γ-TiAl and α_2-Ti_3Al are $a = b = 3.99$ Å, $c = 4.07$ Å, and $a = 5.75$ Å, $c = 4.65$ Å, respectively,

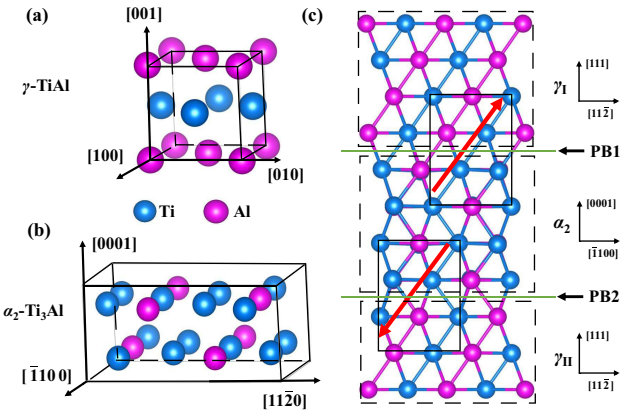


Fig. 1. (a)–(b) Crystal structures of γ-TiAl and α_2-Ti_3Al, respectively. (c) Coherent γ-TiAl (111)/α_2-Ti_3Al (0001) lamellar models containing two types of phase boundaries (PB1 and PB2).

which are consistent with the experimental values.[38] We established two-phase $\gamma_{\rm I}$-TiAl/α_2-Ti_3Al/$\gamma_{\rm II}$-TiAl models containing two types of γ/α_2 phase boundaries (PBs), where the in-plane $[1\bar{1}0]_{\gamma_{\rm I}} \parallel [11\bar{2}0]_{\alpha_2} \parallel [1\bar{1}0]_{\gamma_{\rm II}}$, $[11\bar{2}]_{\gamma_{\rm I}} \parallel [\bar{1}100]_{\alpha_2} \parallel [11\bar{2}]_{\gamma_{\rm II}}$, and $[111]_{\gamma} \parallel [0001]_{\alpha_2}$ were parallel to the *x*-, *y*-, and *z*-axes, respectively, as shown in Fig. 1(c). The α_2-Ti_3Al slab consists of 4 atomic layers (32 atoms), while each γ-TiAl slab contains 6 atomic layers (48 atoms), resulting in a total of 80 atoms for the full supercell. In PB1, the atomic rows composed only of Ti atoms in TiAl and Ti_3Al are aligned across the interface, whereas they are not aligned in PB2.[39] Moreover, we have taken into account the influence of the Al_{Ti} antisite defect, as shown in Fig. 2. In each supercell, only one Ti atom is substituted by an Al atom among the six distinct substitution sites, corresponding to a defect concentration of approximately 1.25%. The formation energy was determined for all possible Al_{Ti} antisite defect sites, as shown in Fig. 2(b). By analyzing the formation energy, the preferred site for the Al_{Ti} antisite defect was identified as Al3, indicating its stability.

The structure of PB1 and γ-TiAl consists of intrinsic Ti–Ti, Al–Al, and Ti–Al bonds, while the main chemical bonds that resist external deformation are Ti–Ti and Al–Al bonds, as shown in Fig. 3(a). Thus, we used ELF and COHP calculations to analyze the critical Ti–Ti and Al–Al bond characteristics, as shown in Fig. 3. In Fig. 3(a), the Ti–Ti and Al–Al bonds in PB1 and γ-TiAl are typical metallic bonds due to their low electron localization values. Moreover, -ICOHP can quantitatively measure the strength of chemical bonds, and the higher the -ICOHP value, the stronger the chemical bond.[40,41] Figure 3(c) shows that the –ICOHP values of Ti–Ti and Al–Al bonds in γ-TiAl (1.13 eV and 2.05 eV, respectively) are both larger than those in PB1 (1.08 eV and 1.92 eV, respectively), indicating a stronger ability to resist external deformation. The Ti–Al covalent bond in γ-TiAl is also stronger than that in PB1, as shown in Fig. S1.

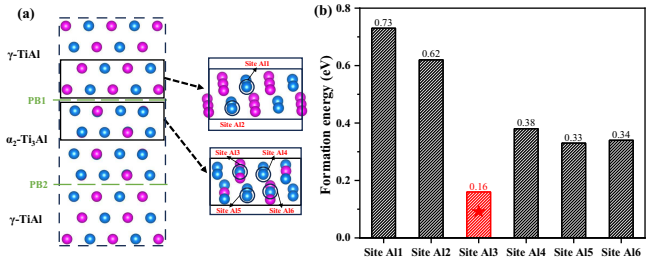


Fig. 2. (a) Schematic of the γ/α_2 lamellar structure with six possible Al_{Ti} antisite defect sites in different components: γ-TiAl, α_2-Ti_3Al, and PB. (b) Formation energy for Al doping in the γ/α_2 lamellar structure.

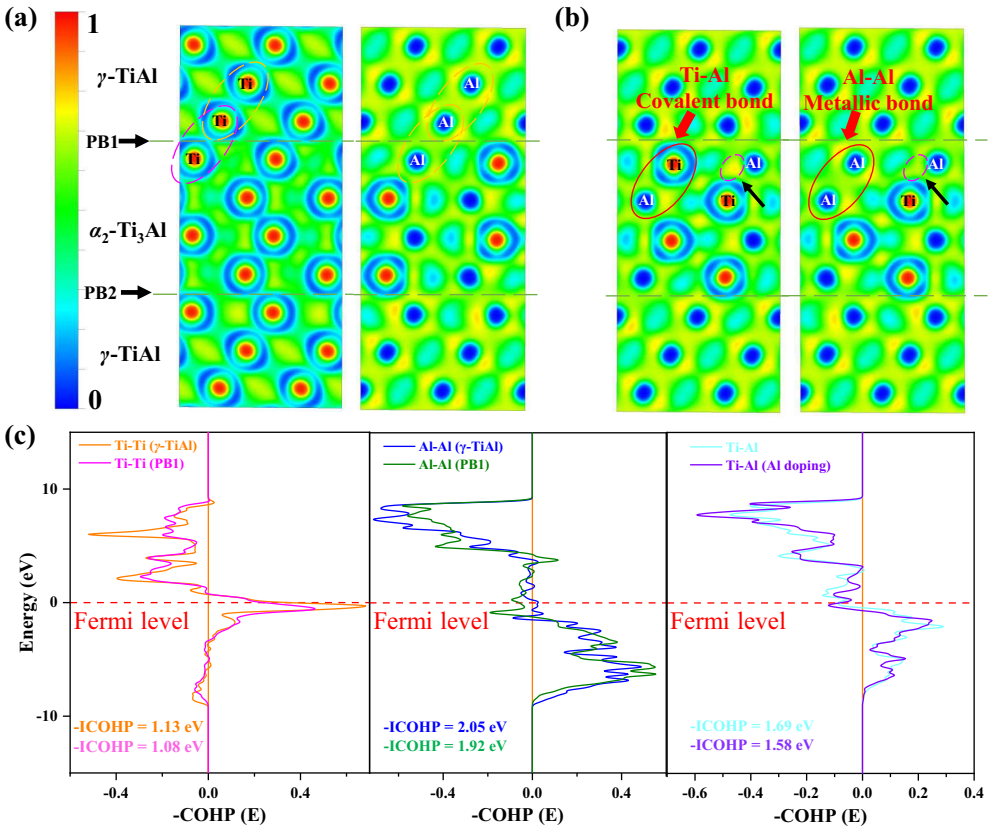


Fig. 3. (a) Front-view ELF sections of the γ/α_2 lamellar structure across different crystallographic planes. (b) Front-view ELF sections of the γ/α_2 layered structures before and after the introduction of the Al_{Ti} antisite defect. (c) The –COHP/–ICOHP values of critical Ti–Ti and Al–Al bonds in PB1 and γ-TiAl, as well as those of Ti–Al bonds before and after the introduction of the Al_{Ti} antisite defect in α_2.

As for α_2-Ti_3Al, we find that the main chemical bonds that resist external deformation along the easy slip system of $1/6[1\bar{1}00]$ basal stacking faults are Ti–Al covalent bonds with highly localized electrons, as shown in Fig. 3(b). In our previous work, the high strength of TiAl alloys was attributed to the high-strength Ti–Al covalent bond.[16] Thus, the intrinsic strength of α_2-Ti_3Al to resist external deformation would be higher than that of γ-TiAl, which means that the deformation mechanism of α_2-Ti_3Al would occur after that of γ-TiAl in the γ/α_2 lamellar structure. In addition, the effect of the Al_{Ti} antisite defect in the γ/α_2 lamellar structure is significant, and we have confirmed the site preference of Al doping in the previous section, whose ELF section in the front view is shown in Fig. 3(b). At the red arrow in Fig. 3(b), we find that a chemical bond in the γ/α_2 lamellar structure (Al_{Ti}) changes from a high-strength Ti–Al covalent bond to an Al–Al metallic bond. The degree of charge localization of the Ti–Al covalent bond in the same layer is reduced by Al doping, as shown by the black arrow in Fig. 3(b). The -ICOHP value of the Ti–Al covalent bond decreases from 1.69 eV to 1.58 eV, as shown in Fig. 3(c), indicating that the strength of the Ti–Al covalent bond in the same layer decreases due to the effect of the Al_{Ti} antisite defect.

In conclusion, the main Ti–Ti and Al–Al chemical bonds that resist deformation in γ-TiAl are stronger than those in PB1. The main chemical bonds that resist deformation in α_2-Ti_3Al are high-strength Ti–Al covalent bonds. The results show the sequence of the deformation mechanism during shear loading. Moreover, the Al_{Ti} antisite defect has weakened the ability of the interlayer to resist deformation, which indicates a plastic strengthening mechanism in $\gamma//\alpha_2$ lamellar structure.

4. Result and discussion

4.1. Deformation mechanisms of γ/α_2 lamellar structure with Al_{Ti} antisite defect

According to the calculation of the formation energy, we constructed a γ/α_2 lamellar structure with an Al_{Ti} antisite defect to study the competitive deformation mechanisms of the γ/α_2 lamellar structure (Al_{Ti}) under shear loading along the easy slip direction. The stress-strain curve, atomic configuration changes, and dynamic responses of the typical bond lengths during pure shear are shown in Fig. 4. The stress-strain curve of the γ/α_2 lamellar structure without any defect is shown as a red dashed line in Fig. 4(a), with the corresponding competitive deformation mechanisms shown in Fig. S2a. As shown in Fig. 4(a), there are multiple stress mutation processes, and we classify them into three sequential stages: "PB transition", "orientation transition" in γ-TiAl, and "phase transition" in α_2-Ti_3Al. The peak stress of the "PB transition" is 3.0 GPa, and the "orientation transition" occurs in γ-TiAl at about 5.0 GPa. The stress of the last "phase transition" stage is 7.6 GPa. Moreover, there is a special deformation stage, leading to SISF formation in γ-TiAl and a phase transition in α_2-Ti_3Al (Al_{Ti}) simultaneously.

The γ-TiAl/α_2-Ti_3Al lamellar structure (Al_{Ti}) remained intact after stress mutation, with chemical bonds broken and reformed. The atomic configurations of the γ/α_2 lamellar structure (Al_{Ti}) during shearing, along with the corresponding chemical bond lengths, are shown in Figs. 4(b) and 4(c). From strains of 0 to 0.09, the lamellar structure was uniformly deformed to resist shear deformation. The State 2 (strain 0.10) in Fig. 4(b) shows atomic configurations after the first stress mutation, with the main Ti–Ti and Al–Al bonds broken and reformed, which results in the "PB transition". As shown in Fig. 4(c), the Ti–Ti bond length changes from 3.05 Å to 4.02 Å, with an increase of $\sim 30\%$, indicating bond breakage. The low strength of 3.0 GPa for the "PB transition" means that it can be easily activated to create slip pathways for ductility. With increasing strain, the deformation mechanism of the "orientation transition" in γ-TiAl is the SISF process (SISF formation, migration, and annihilation) from State 2 to State 6. The atomic configuration changes involve repeated slipping of the γ-TiAl phase along the $1/6[11\bar{2}]$ Burgers vector on the (111) surface, accompanied by the breaking of Ti–Ti and Al–Al bonds between layers and the generation of new Ti–Ti and Al–Al bonds. Thus, the structure of γ-TiAl finally becomes a hard slip system of $(111)/[\bar{1}\bar{1}2]$. The strength of the "orientation transition" is ~ 5.0 GPa, and the continuous interlayer slip in γ-TiAl results in the excellent ductility of the γ/α_2 lamellar structure by dissipating strain energy. As shown in Fig. 4(b) for State 7 (strain 0.95), the deformation mechanism of the last stress mutation is "phase transition" with a high strength of 7.6 GPa, which causes the α_2-Ti_3Al phase to change from a hexagonal close-packed (HCP) structure to a face-centered cubic (FCC) structure due to the $1/6[1\bar{1}00]$ incomplete dislocation in α_2-Ti_3Al. In addition, from State 3 (strain 0.22) to State 4 (strain 0.40), there is a special deformation mechanism of "phase transition" that occurs between layers where the Al_{Ti} antisite defect exists. The stress of this special deformation stage is approximately 5.0 GPa, which means that the strength of the phase transition in this special stage is similar to that of the SISF process owing to the effect of the Al_{Ti} defect. Ultimately, the structure of the Al-doped γ/α_2 lamella becomes a full FCC structure. Due to the effect of the Al_{Ti} defect, the incomplete "phase transition" occurs during "orientation transition", which provides additional low-energy slip paths for atomic rearrangement under applied shear, effectively delaying structural instability. The shear strain of the γ/α_2 lamellar structure (Al_{Ti}) increased to 0.93 from 0.78, contributing to a $\sim 19\%$ enhancement in plasticity.

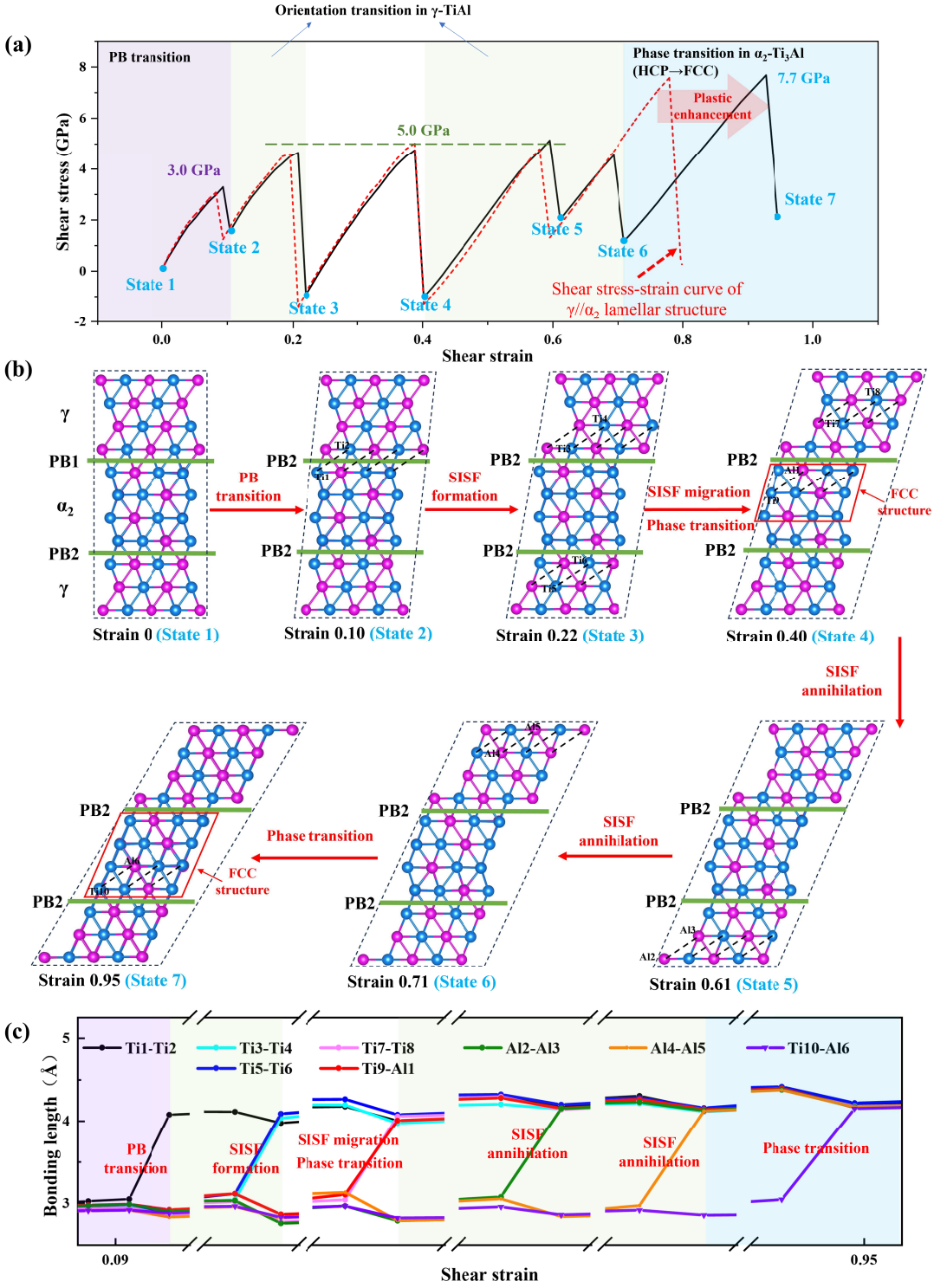


Fig. 4. Deformation mechanisms of the γ/α_2 lamellae structure (Al_{Ti}) under shear loading. (a) Shear stress-strain relationship during shearing. (b) Intact atomic structure of the γ/α_2 lamellae structure (Al_{Ti}) at strain 0 and atomic configurations after stress release at strains 0.10, 0.22, 0.40, 0.61, 0.71, and 0.95, respectively. (c) Dynamic responses of typical bond lengths as a function of shear strain.

4.2. Energy explanation of the deformation competitive mechanisms

During pure shear in the γ/α_2-Ti_3Al lamellar structure (Al_{Ti}), according to the shear stress-strain relationship and atomic configuration changes, there are three deformation stages: "PB transition", "orientation transition", and "phase transition". As shown in Fig. 4(a), we found that the sequence of the three deformation stages is related to their strength; the lower the strength, the earlier the stage occurs. To reveal the intrinsic mechanical behavior, we calculated the generalized stacking fault energy (GSFE) of possible competitive deformation mechanisms. As shown in Fig. 5(a), there is a schematic of possible slip directions under pure shear loading in the γ/α_2 lamellar structure (Al_{Ti}), and G1, G2, G3, G3(Al),

and G4 are the possible deformation modes in PB1, γ-TiAl, α_2-Ti_3Al, and PB2, respectively. Figure 5(b) shows the GSFE curves with different displacements during the deformation process, where we found that the lowest slip energy barrier is 177.0 mJ/m^2 when the structure slips in PB1 (G1) of the γ/α_2 lamellar structure. The slip energy barrier in γ-TiAl (G2) is 299.6 mJ/m^2. The slip energy barrier of 476.6 mJ/m^2 in α_2-Ti_3Al (G3) is larger than that in γ-TiAl and PB1. The highest slip energy barrier of 1135.0 mJ/m^2 in PB2 (G4) indicates that it is difficult to slip, demonstrating that the presence of PB2 strengthens the γ-TiAl/α_2-Ti_3Al lamellar structure. The slip energy barrier of the phase transition decreases to 282.7 mJ/m^2 (G3(Al_{Ti})), which occurs in the layers where the Al_{Ti} antisite defect exists in α_2-Ti_3Al. This slip energy barrier is as low as that of γ-TiAl (G2).

Therefore, during pure shear in the γ/α_2 lamellar structure, interlayer slipping occurs in PB1, γ-TiAl, and α_2-Ti_3Al, and the interlayer in α_2-Ti_3Al (Al_{Ti}) slips together with γ-TiAl, providing an enhancement in plasticity. Moreover, the interlayer slipping in PB1 leads to a PB transition based on atomic configuration analysis (PB1 to PB2), which strengthens the interfacial strength of the phase boundary owing to its high slip energy barrier of 1135.0 mJ/m^2.

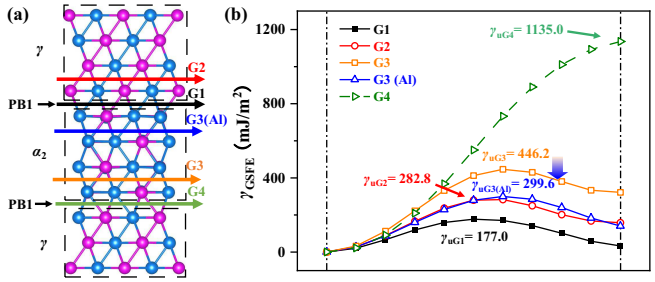


Fig. 5. (a) Schematic of possible slip systems under pure shear loading in the γ/α_2 lamellar structure (Al_{Ti}). (b) Calculated generalized stacking fault energies of the γ/α_2 lamellae for possible competitive mechanisms among deformation modes during pure shear. The arrow directions of G1 and G4 indicate the force directions of PB1 and PB2, respectively, when they resist deformation. The arrow directions of G2 and G3 are the easy slip directions for γ-TiAl and α_2-Ti_3Al, respectively, during shear loading. In addition, G3(Al) is an easy slip direction for α_2-Ti_3Al after the introduction of the Al_{Ti} antisite defect.

5. Conclusion

The competitive deformation mechanisms and the relationship between the structure-related chemical bond characteristics of the γ-TiAl/α_2-Ti_3Al lamellar structure were thoroughly investigated. The main research results are as follows:

(i) The deformation mechanisms of the γ/α_2 lamellar structure under pure shear mainly contain three sequential stages: "PB transition" in PB1, "orientation transition" in γ-TiAl, and "phase transition" in α_2-Ti_3Al. Their shear strengths are 3.0 GPa, 5.0 GPa, and 7.6 GPa, respectively. The sequence of these stages depends on the comparison of bond strengths.

(ii) Introducing an Al_{Ti} antisite defect can weaken the original Ti–Al covalent bond while generating a new Al–Al metallic bond. This provides an additional slip path for the γ/α_2 lamellar structure that dissipates strain energy, resulting in a $\sim$ 19% enhancement in plasticity.

(iii) The competition mechanisms between these plastic behaviors can be well explained through GSFE calculations. The presence of PB2 strengthens the γ/α_2 lamellar structure owing to its high slip energy barrier of 1135.0 mJ/m^2.

Acknowledgment

Project supported by the National Natural Science Foundation of China (Grant Nos. 92163215, 92163212, 92463301, and 92463309).

References

[1] Chen Y, Yao Z H, Dong J X, Yang H Y, Ren M, Peng J L, Leng L X, Zhang X M and Yang J M 2024 *Mater. Charact.* **213** 12
[2] Li B Q, Zhou H G, Liu J F and Kang C 2021 *Aerosp. Sci. Technol.* **119** 15
[3] Li D W, Liu J X, Sun Y T, Huang W Q, Li N and Yang L H 2023 *J. Alloys Compd.* **957** 12
[4] Li Z X, Li S W, Peng Y, Zhang Y M, Guo W, Xiong J T and Li J L 2022 *J. Manuf. Process.* **84** 1331
[5] Sun D B, Ma G L, Wan Z H and Gao J H 2023 *Eng. Fail. Anal.* **154** 16
[6] Wang M S, Du Y L, Wei H L and Liao W H 2023 *Mater. Des.* **231** 17
[7] Wang Q, Wu X L, Liu X W, Zeng L C, Ding H S, Chen R R and Guo J J 2023 *J. Alloys Compd.* **947** 11
[8] Yim S, Bian H K, Aoyagi K, Yanagihara K, Kitamura S I, Manabe H, Daino Y, Hayasaka Y, Yamanaka K and Chiba A 2022 *Addit. Manuf.* **51** 16
[9] Zhang X Y, Li C W, Wu M H, Ye Z H, Wang Q and Gu J F 2022 *Acta Mater.* **227** 15
[10] Zhang X Y, Li C W, Zheng M Y, Yang X D, Ye Z H and Gu J F 2022 *J. Mater. Sci. Technol.* **117** 99
[11] Mayer S, Erdely P, Fischer F D, Holec D, Kastenhuber M, Klein T and Clemens H 2017 *Adv. Eng. Mater.* **19** 1600735
[12] Hamrani A, Bouarab F Z, Agarwal A, Ju K and Akbarzadeh H 2023 *Virtual Phys. Prototyp.* **18** e2273303
[13] Chen G, Peng Y B, Zheng G, Qi Z X, Wang M Z, Yu H C, Dong C L and Liu C T 2016 *Nat. Mater.* **15** 876
[14] Ma Y L, Yang J R, Liu Z D and Chen R R 2024 *Mater. Sci. Eng. A* **915** 16
[15] Dey S R, Hazotte A, Bouzy E and Naka S 2005 *Acta Mater.* **53** 3783
[16] Sheng L, Zhai P C, Huang X G, Ma H Q, Huang B, Li W J, Chen G, Duan B, Feng X B and Li G D 2025 *J. Alloys Compd.* **1010** 9
[17] Wu X L, Yang M X, Yuan F P, Wu G L, Wei Y J, Huang X X and Zhu Y T 2015 *Proc. Natl. Acad. Sci. USA* **112** 14501
[18] Wu X L, Yang M X, Yuan F P, Chen L and Zhu Y T 2016 *Acta Mater.* **112** 337
[19] Chen Y, Cao Y D, Qi Z X and Chen G 2021 *J. Mater. Sci. Technol.* **93** 53
[20] Ji Z W, Lu S, Hu Q M, Kim D, Yang R and Vitos L 2018 *Acta Mater.* **144** 835
[21] Zhou X, Wang S P, Lu Z T, Huang X G, Feng X B, Fu J Y, Li W J, Zhai P C and Li G D 2025 *Acta Mech. Sin.* **41** 6
[22] Xiang H G and Guo W L 2022 *Int. J. Plast.* **150** 14
[23] Xu X S, Ding H S, Huang H T, Liang H, Kawk S, Chen R R, Guo J J and Fu H Z 2021 *J. Mater. Res. Technol.* **14** 2884
[24] Li L, Zhao W, Feng Z X, Sun J and Li X Q 2020 *Trans. Nonferrous Met. Soc. China* **30** 2143
[25] Gabrisch H, Lorenz U, Pyczak F, Rackel M and Stark A 2017 *Acta Mater.* **135** 304
[26] Rackel M W, Stark A, Gabrisch H and Pyczak F 2021 *Intermetallics* **131** 107086
[27] Rackel M W, Stark A, Gabrisch H, Schell N, Schreyer A and Pyczak F 2016 *Acta Mater.* **121** 343

[28] Zhao Z Q, Chu L L, Yu M L, Guo W L and Zhang Z H 2024 *Adv. Funct. Mater.* **34** 34
[29] Wang T M, Wang B Y, Ju X, Gu Q, Wang Y X and Gao F 2001 *Chin. Phys. Lett.* **18** 361
[30] Audouze C, Jollet F, Torrent M and Gonze X 2006 *Phys. Rev. B* **73** 18
[31] Kresse G and Furthmüller J 1996 *Phys. Rev. B* **54** 11169
[32] Li G D, An Q, Li W J, Goddard W A III, Zhai P C, Zhang Q J and Snyder G J 2015 *Chem. Mater.* **27** 6329
[33] Li G D, An Q, Morozov S I, Duan B, Goddard W A III, Zhai P C, Zhang Q J and Snyder G J 2018 *Scr. Mater.* **157** 90
[34] Li G D, Aydemir U, Duan B, Agne M T, Wang H T, Wood M, Zhang Q J, Zhai P C, Goddard W A III and Snyder G J 2017 *ACS Appl. Mater. Interfaces* **9** 40488
[35] Maintz S, Deringer V L, Tchougréeff A L and Dronskowski R 2013 *J. Comput. Chem.* **34** 2557
[36] Maintz S, Deringer V L, Tchougréeff A L and Dronskowski R 2016 *J. Comput. Chem.* **37** 1030
[37] Momma K and Izumi F 2008 *J. Appl. Crystallogr.* **41** 653
[38] Pearson W B 1958 *A Handbook of Lattice Spacings and Structures of Metals and Alloys* (London: Pergamon))
[39] Inui H, Nakamura A, Oh M H and Yamaguchi M 1991 *Ultramicroscopy* **39** 268
[40] Noda H, Sakaguchi S, Fujita R, Minami S, Hirakata H and Shimada T 2025 *Acta Mater.* **287** 120795
[41] Zhang G, Chen G, Panwisawas C, Teng X, An R, Cao J, Huang Y, Dong Z and Leng X 2024 *Acta Mater.* **281** 120426